Multiple Intermediates in the Detergent-Induced Fusion of Lipid Vesicles

L. G. Dresser[1], C. Kunstmann[1,a], D. Conteduca[1,b], S. Johnson[1,2], J. C. Penedo[3,4], M. C. Leake[1,2,5] & S. D. Quinn[1,2*]

[1]School of Physics, Engineering and Technology, University of York, Heslington, York, YO10 5DD.

[2]York Biomedical Research Institute, University of York, Heslington, York, YO10 5DD.

[3]Centre of Biophotonics, School of Physics and Astronomy, University of St Andrews, North Haugh, St Andrews, Fife, KY16 9SS.

[4]Biomedical Sciences Research Complex, University of St Andrews, North Haugh, St Andrews, Fife, KY16 9ST.

[5]Department of Biology, University of York, Heslington, York, YO10 5DD.

[a]Current Location: University of Southern Denmark, Campusvej 55, 5230, Odense, Denmark.

[b]Current Location: Massachusetts General Hospital, 55 Fruit Street, Boston, Massachusetts, 02114, USA.

*steven.quinn@york.ac.uk

Abstract

The structure, dynamics and function of lipid vesicles are heavily influenced by a range of physical forces, local microenvironmental effects and interactions with perturbative molecules, including detergents. Detergent-induced membrane interactions – critical for a wide range of applications including protein extraction and virus inactivation – varies in magnitude according to the detergent type and membrane composition, but the underlying mechanistic details remain largely under explored. Open questions relate to the precise molecular-level pathway of detergent-induced vesicle fusion, the nature of the fusion products, the influence of modulatory factors, and whether fusion states can be controllably harnessed for bionanotechnology. By using a lipid mixing assay based on Förster resonance energy transfer (FRET), and single-vesicle characterization approaches to assess vesicle heterogeneity, we identify that both freely-diffusing and surface-tethered sub-micron sized vesicles are induced to fuse by the widely-used non-ionic detergent Triton-X 100. We demonstrate that the fusion process is a multi-step mechanism, characterized by discrete values of FRET efficiency between membrane-embedded donor and acceptor fluorophores, and involves vesicle docking, hemi-fusion and full lipid mixing, even at sub-solubilizing detergent concentrations. We present evidence that the fusion process is regulated by environmental factors including membrane composition and phase, and we dissect the kinetics of vesicle fusion in contact with solid surfaces using a label free quartz-crystal microbalance with dissipation monitoring approach. The presented strategies are likely to be applicable beyond the vesicle sizes and compositions studied

here, and not only provide mechanistic insight into the multifaceted dynamics of vesicle fusion but also have implications for a wide range of biotechnological applications including drug delivery, sensor development, surfactant sensing, biomimetic formation, and microfluidics, where transport and manipulation of encapsulated cargo is essential.

Introduction

Detergent-membrane interactions are critical for biotechnological applications including membrane-protein extraction[1, 2], cell lysis[3], targeted drug delivery[4], and virus inactivation[5, 6]. In this context, the widely-used non-ionic detergent Triton X-100 (TX-100) plays a key role by efficiently and effectively solubilizing membrane bilayers and exposing their hydrophobic cores. Open questions regarding the interaction, which involves membrane fusion as a key component[7, 8, 9], include elucidating the detergent's precise molecular-level mode of action, its role in lipid-lipid interactions, the nature and morphology of the fused species, and establishing the influence of cofactors and environmental conditions that modulate the process.

Thermodynamic approaches aimed at characterizing the TX-100-membrane interaction have typically used highly-controllable model-membrane systems such as supported bilayers or synthetic unilammelar vesicles (UVs) to unveil concentration requirements necessary for solubilization[10], and to disentangle the influence of membrane phase, composition, charge, and detergent: lipid ratio on the interaction[11]. In this context, UVs are classified as small (SUVs), large (LUVs) or giant (GUVs) reflecting vesicle sizes of < 100 nm, 100 nm -1 μm and > 1 μm respectively. GUVs in particular have played a key role in interrogating the TX-100 membrane interaction[12] with measurements broadly confirming that TX-100 induces solubilization at concentrations above its critical micellar concentration (CMC). However, dynamic light scattering (DLS) and turbidity approaches have also revealed an intriguing growth in vesicle size under sub-solubilizing conditions[7, 8, 9, 13], pointing towards morphological changes such as membrane swelling and fusion[8] that could be harnessed for biotechnological applications.

To assess the swelling aspect, single-vesicle characterization approaches based on the fluorescence imaging of GUVs have revealed detergent-induced surface-area enhancements concurrent with the formation of dynamic pores[14, 15, 16]. Similar work also revealed that the membrane tension on both micron- and 100 nm-diameter vesicles decreases with TX-100 concentration, and the detergent introduces phase separation events in vesicles incorporating modest concentrations of cholesterol[16, 17]. More recently, we demonstrated that variations in the efficiency of Förster resonance energy transfer (FRET) between fluorescently labelled lipids in LUVs quantitatively reports on their expansion upon TX-100 addition[18], and combinations of molecular dynamics simulations and fluorescence approaches have revealed dynamic membrane bending events and the formation of local invaginations all prior to micellization[19].

These results, and others[20], are broadly supportive of a dynamic model for TX-100 induced membrane solubilization that involves detergent saturation on the membrane surface, the formation of mixed detergent-lipid micelles, structural changes within the intact membrane, and the release of mixed micelles to solution. A more quantitative extension of this model involves the formation of phase- and composition-sensitive pores, content leakage, variations in membrane curvature and local changes to the bilayer fluidity[21]. However, the molecular mechanisms underpinning another major class of event - namely TX-100 induced vesicle fusion - are not well characterized owing in part to a lack of experimental techniques capable of capturing the entire process.

In the context of vesicle fusion, optical microscopy experiments based on the imaging of unlabelled GUVs incubated with fluorescently-tagged native membranes at sub-solubilizing TX-100 concentrations have indicated the presence of fusion by the appearance of fluorescence at the GUV site[22]. Using similar approaches, fusion between proteoliposomes and native membranes has been harnessed to enable reconstitution of transmembrane proteins into GUV bilayers after TX-100 addition[7, 8, 9, 23]. Phase contrast imaging and DLS measurements also indicate that the degree of fusion is dependent on the lipid composition, suggesting that the TX-100-membrane interaction may be a much more complex and multifaceted process. Confocal-based fluorescence experiments have also been employed to assess permeable GUV fusion, and although fusion was rarely observed, the results point towards a situation where fusion can occur due to casual contact between pores on adjacent membranes[15]. Unfortunately, conventional microscopy techniques are limited in their ability to resolve structural changes in objects smaller than 5-10 μm, can only quantify macroscopic changes in size and packing density and they lack the ability to follow molecular-level structural rearrangements on the nanoscale. There is therefore demand for alternative methods that can monitor the fusion of individual vesicles with sizes comparable to LUVs. In this regard, molecular dynamics simulations have alluded to a stock-pore mechanism of spontaneous bilayer fusion where initial vesicle docking precedes the formation of an hourglass-shaped connection between two adjoining membranes before hemi-fusion and full lipid mixing[15, 24, 25]. Whether such a mechanism occurs in detergent-rich media, and whether these states can be controllably harnessed remains an open question.

Inspired by these insights and in search of the mechanistic origins of TX-100 induced vesicle fusion, we adopted a range of ensemble- and single-vesicle characterization approaches to interrogate the structural integrity of highly-curved LUVs composed of POPC (1-palmitoyl-2-oleoylglycero-3-phosphocholine) in response to TX-100. The LUVs used here differ from low-curvature GUV species by displaying a maximal principal curvature[26] of ~$10^7 m^{-1}$, which is an order of magnitude greater than those typically observed in GUVs. By employing isothermal titration calorimetry and particle sizing approaches including DLS and fluorescence correlation spectroscopy (FCS), we first confirm an enhancement in vesicle radius under sub-solubilizing conditions. We next showcase a steady-state and time-resolved assay based on Förster resonance energy transfer (FRET)[27, 28], to quantitatively assess the degree of TX-100 induced lipid mixing between vesicles. Based on the magnitude of the observed FRET efficiency between fused vesicles, coupled with morphological changes observed via electron microscopy approaches, we reveal that the detergent-induced fusion process is a time-dependent and multi-step process comprising vesicle docking, hemifusion and full lipid mixing prior to solubilization. While we have previously used FRET-based methods to quantitatively report on vesicle swelling[18, 29, 30], here we take advantage of stepwise enhancements in the FRET efficiency to quantify the magnitude and state of fusion. To further characterize the interaction, we also deploy a calcium-sensing assay to assess and confirm content exchange between fusing vesicles. Finally, to demonstrate the potential of TX-100 to facilitate vesicle fusion in contact with solid surfaces, and to extract kinetic details of the process, we deployed an acoustic-sensing approach based on quartz-crystal microbalance with dissipation monitoring (QCM-D). In this regard, the QCM-D approach offers highly-sensitive real-time monitoring of surface mass and viscoelasticity, without the need for fluorescent labels. This not only opens exciting possibilities for the controllable delivery of encapsulated cargo to a substrate but may also support a range of bionanotechnological applications including diagnostic sensing, drug delivery and the formation of biomaterials.

Our discovery of a multi-step and controllable fusion process in both freely-diffusing and surface-tethered vesicles at sub-solubilizing detergent concentrations provides new clues to the underlying TX-100-membrane interaction and may have important implications for the transport of membrane proteins such

as proton pumps and transport receptors[22]. We also expect the presented techniques to have general applicability for assessing interactions between highly curved lipid vesicles and a wide range of fusogens, such as neurotoxic proteins with important biomedical significance.

Results

Triton X-100 Alters the Morphology of Vesicles at Sub-Solubilizing Concentrations

LUVs composed of POPC lipids were first prepared by the extrusion method and confirmed to be ~200 nm in diameter by DLS (**Figure S1**). To explore the thermodynamic parameters of the TX-100-LUV interaction, and to assess the critical micellar concentration of TX-100 in solution, we employed isothermal titration calorimetry (ITC). As previously indicated, ITC is a tool of choice for assessing the heat associated with surfactant induced membrane solubilization[31], and is widely accepted as a reliable ensemble approach for evaluating solubilization and critical micellar conditions[31]. Here, 10 μL aliquots of TX-100 from a 5 mM stock solution were progressively titrated into solution containing vesicles at a final lipid concentration of 88 μM. We observed that each injection triggered a temporary decrease in the applied power, consistent with an exothermic process involving detergent partitioning into the vesicle bilayer (**Figure 1a**). As fewer vesicles became available for interaction, either through saturation of TX-100 or by solubilization, each subsequent injection of TX-100 reduced the number of available interaction sites, as measured by a decrease in the corresponding integrated reaction enthalpies, ΔH, after baseline subtraction (**Figure 1a**). Injections leading up to a TX-100 concentration of 0.25 mM resulted in a 30 % increase in ΔH, suggestive of vesicle-detergent interactions at concentrations below the reported critical micellar concentration - a finding that warranted further attention given non-ionic surfactants typically only achieve membrane solubilization once above the CMC. When solubilization was complete, only a heat signal resulting from mixing, dilution effects and liquid friction was observed. To quantify the TX-100 CMC directly under the solutions conditions used, we titrated TX-100 directly into buffer solution lacking vesicles and identified a CMC of 0.25 mM, defined as the midpoint of the sigmoidal ΔH transition curve, and identified by the peak of its first-order derivative[31] (**Figure S2**).

We next employed FCS and DLS to assess detergent-induced morphological changes across the interaction. Both techniques are sensitive to the diffusion coefficient of freely diffusing vesicles in solution, and thus quantitatively report on their hydrodynamic radius via the Stokes-Einstein relationship[32]. The FCS correlation curves associated with freely diffusing LUVs labelled with 0.1 % of the fluorescent membrane dye DiI progressively shifted towards longer lag times at detergent concentrations below the CMC. Here, a reduction of 40 % in vesicle diffusion coefficient, from an initial starting value of 1.28 ± 0.01 $\mu m^2 s^{-1}$ (±SD) in the absence of TX-100, was observed (**Figure 1b**), corresponding to an increase in hydrodynamic diameter (d_H) from 168 ± 1 nm to 290 ± 5 nm. In line with previous work[18], we attributed these observations to vesicle swelling, docking, fusion, aggregation, or combinations of these effects in solution. At TX-100 concentrations beyond the CMC, the particle radius reduced to ~3.5 nm which we assigned to solubilization and the formation of mixed detergent-lipid micelles. DLS also confirmed a positive shift in size distribution, though we note in these experiments, the lipid concentration was increased by two orders of magnitude relative to the FCS work, which we hypothesised could facilitate fusion. Here, correlation curves obtained from the intensity of scattered light also progressively shifted towards longer lag times (**Figure 1c**). Without detergent, the vesicles displayed a lognormal size distribution, as expected for freely diffusing species, peaking at 182 nm with a low polydispersity index of 0.16 ± 0.01 (**Figure 1d, Figure S3**). At detergent concentrations approaching the CMC, the correlation curves then revealed a 1.7-

fold increase in vesicle size (**Figure 1d**) and ~4-fold increase in polydispersity index (**Figure S3**), suggestive of mixed species in the ensemble.

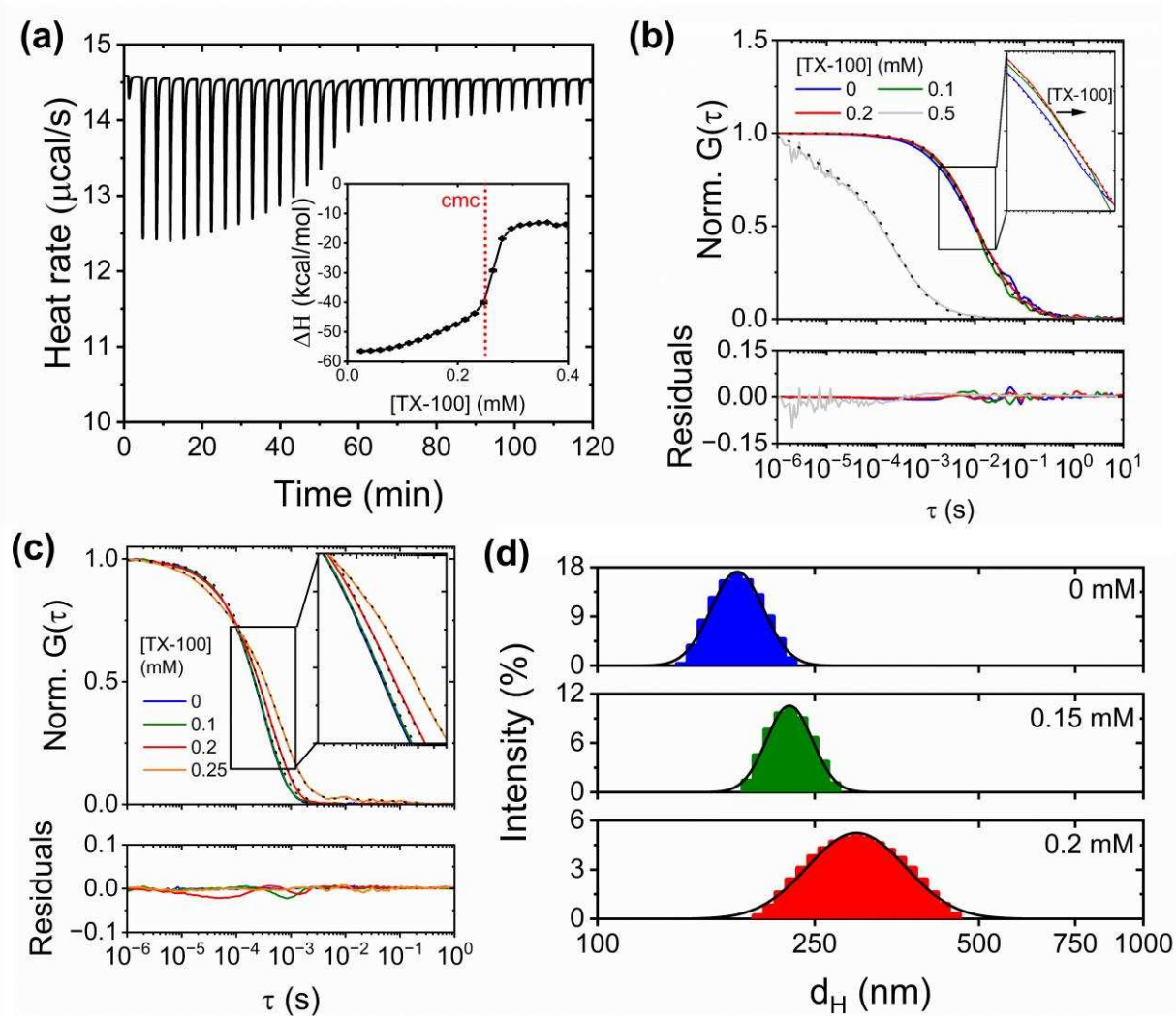

Figure 1. Characterization of vesicle-detergent interactions at sub-solubilizing TX-100 concentrations. (a) Heat flow versus time recorded via ITC as a 5 mM solution of TX-100 is injected into solution containing LUVs. Inset: integrated reaction enthalpies per injection. The dashed red line corresponds to the CMC of TX-100 under the solution conditions used. (b) Top: Normalized variation in FCS correlation curves (solid lines) and fits (dotted lines) associated with interactions between LUVs and 0 (blue), 0.1 (green), 0.2 (red) and 0.5 (grey) mM TX-100. Bottom: corresponding residuals of the fits. (c) Top: Normalized variation in DLS correlation curves (solid lines) and fits (dotted lines) associated with interactions between LUVs and 0 (blue), 0.1 (green), 0.2 (red) and 0.25 (orange) mM TX-100. Bottom: residuals of the fits. (d) Hydrodynamic diameter distributions obtained from LUVs in the absence (blue) and presence of 0.15 (green) and 0.2 (red) mM TX-100. The solid black lines represent lognormal fits with peak d_H values of 182.6 ± 0.1 nm (Chi-squared χ_r^2 = 0.02) (top), 226.8 ± 0.2 nm (χ_r^2 = 0.02) (middle) and 311.2 ± 0.7 nm (χ_r^2 = 0.01) (bottom), respectively.

Triton X-100 Induces Vesicle Fusion

To directly test for fusion, we next employed a lipid mixing assay to monitor interactions between LUVs containing 2 % DiI (FRET donor) and those containing 2 % DiD (FRET acceptor) (**Figure 2a**). Direct excitation of DiI in the absence of fusion thus yields low sensitized emission from the acceptor, however, upon vesicle fusion, lipid mixing brings the FRET pairs into close proximity, triggering enhanced sensitized acceptor

emission as a consequence of non-radiative energy transfer[27, 28, 33]. A key benefit of the approach is that the total number of fluorophores remains constant throughout the fusion process, allowing for intermediate states, corresponding to different levels of lipid mixing, to be observed by quantifiable variations in the FRET efficiency. Ensemble FRET measurements were performed as an initial step to quantify interactions between DiI and DiD coated vesicles in response to TX-100. Here, we measured the efficiency of energy transfer using the RatioA parameter which compares the amount of sensitized acceptor emission with that obtained by direct excitation of the acceptor. In the absence of TX-100 the intensity of sensitized acceptor emission obtained from a 1: 3 mixture of DiI: DiD vesicles was minimal, then progressively increased upon TX-100 addition towards the CMC, and was anti-correlated with quenching of the donor (**Figure 2b**, **Figure S4**). Beyond the CMC, the apparent FRET efficiency then decreased towards its initial value, reflected by an enhancement of the donor signal and corresponding reduction in sensitized acceptor emission (**Figure 2b, Figure S4**). The data therefore supports a situation where progressive addition of TX-100 below the CMC leads to fused vesicle states prior to solubilization and the formation of micelles (**Figure 2c**). Indeed, this is reflected in the RatioA response, where a progressive increase towards a peak of 0.49 ± 0.03 at the CMC was observed, suggestive of morphological changes in the ensemble that results in close proximity of the dyes, followed by a reduction towards its initial value, indicative of solubilization (**Figure 2d**). We note that the amounts of DiI and DiD per vesicle and the DiI: DiD ratio were optimized (1: 3, 2 % of each dye) to maximize the magnitude of the FRET response across the interaction (**Figure S5**).

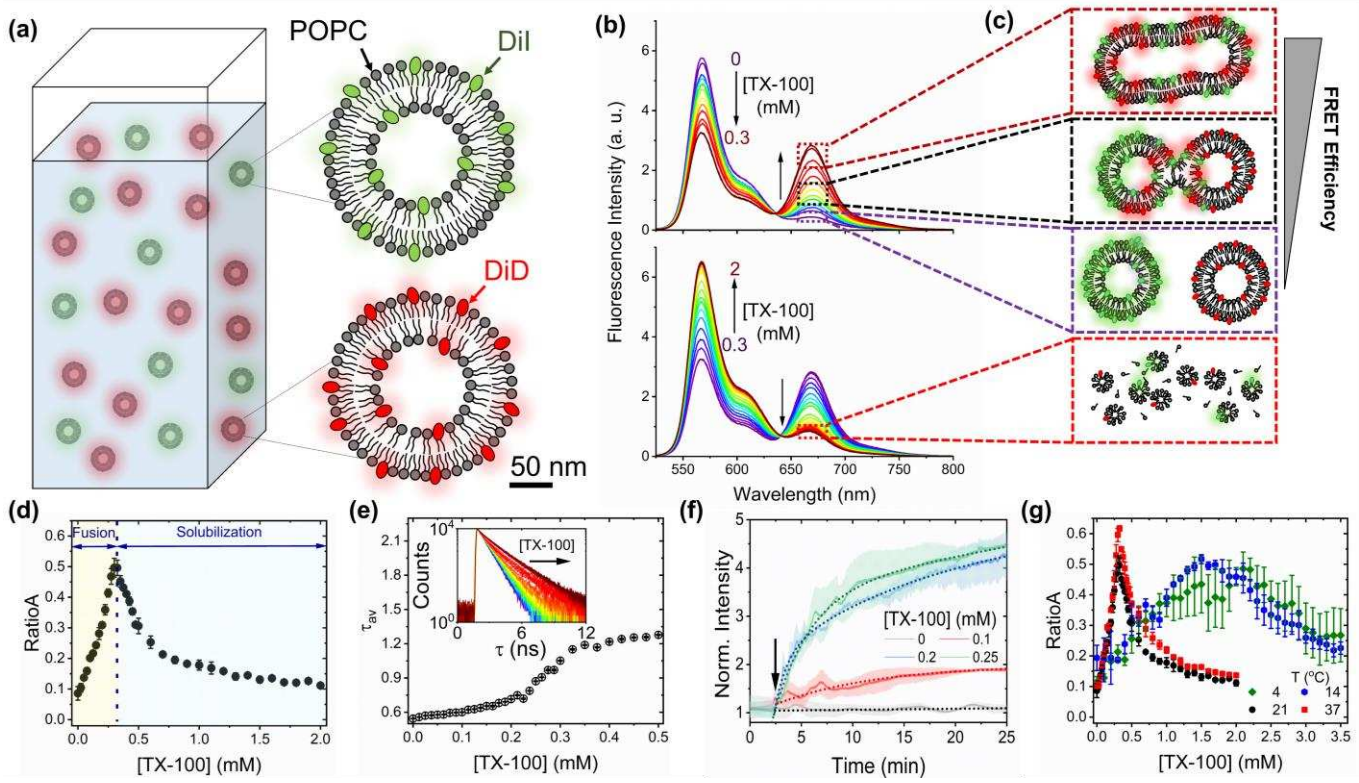

Figure 2. TX-100 induces vesicle fusion. (a) Schematic illustration of the lipid mixing assay. POPC LUVs containing 2 % DiI (green) and 2 % DiD (red) are incubated at a 1: 3 ratio. (b) Representative variation in fluorescence emission spectra (λ_{ex} = 520 nm) obtained from LUVs in the presence of 0 – 0.3 mM (top panel) and 0.3 mM – 2 mM TX-100 (bottom panel). (c) Mixing LUVs with TX-100 results in stepwise FRET enhancements assigned to vesicle docking and fusion prior to stepwise FRET reductions attributed to micellization. (d) Corresponding variation in RatioA and (e) amplitude weighted average lifetime (inset: fluorescence decays) of DiI across the titration. (f) Time-dependent variation in DiD emission upon injection of TX-100 (λ_{ex} =

520 nm). The grey dashed line corresponds to a linear fit and coloured dashed lines correspond to bi-exponential fits. The arrow indicates the point of TX-100 injection. (g) Variation in RatioA as a function of temperature.

To confirm the presence of an energy transfer mechanism between DiI and DiD during the interaction, we also evaluated the amplitude-weighted fluorescence lifetime, τ_{av}, of DiI in the presence of DiD. In all cases, the lifetime decays displayed bi-exponential behaviour after deconvolution with the instrument response function (**Figure S6**), which likely reflects variations in local viscosity across both leaflets[34, 35]. As TX-100 was progressively titrated at concentrations below the CMC, τ_{av}, remained largely unchanged from its initial starting value of ~0.54 ns, then sharply increased towards ~1.2 ns as the concentration of TX-100 increased beyond the CMC (**Figure 2e**). We note that the DiI lifetime in the absence of DiD-labelled vesicles and TX-100 was similar (~0.6 ns) to the initial starting value which we interpreted as evidence of minimal spontaneous fusion prior to injection of TX-100 (**Figure S7**). Similar observations were made when vesicles containing lower concentrations of dye were evaluated (0.1 % DiI and 1 % DiD) (**Figure S7**), though we note that the initial amplitude-weighted average lifetime in the absence of TX-100 was ~2-fold longer (0.94 ns), which may reflect a situation where the in-tact vesicles containing 2 % dye exhibit an initial degree self-quenching. Nevertheless, the faster of the two lifetime components, τ_1, initially decreased at detergent concentrations below the CMC, providing confidence of donor-quenching due to the acceptor, and corresponding increase in FRET efficiency (**Figure S7**), before the solubilization step. In both cases, the subsequent increase in τ_{av}, coupled with reductions in RatioA, which effectively removes contributions from DiI, provide confidence of a TX-100-induced solubilization mechanism comprising stepwise vesicle fusion (high FRET), which may involve docking and hemifusion below the CMC, followed by solubilization and mixed micelle formation above the CMC (low FRET) (**Figure 1c**).

We also note the time-dependent increase in sensitized DiD emission following TX-100 injection followed bi-exponential kinetics, pointing further towards a fusion process involving multiple stages. In the absence of TX-100, DiD emission remained largely invariant across the observation time window, also indicating a lack of spontaneous fusion, however, upon TX-100 addition, bi-exponential kinetics were monitored where the amplitude weighted time constant was 273 ± 6 s in the presence of 0.1 mM TX-100, and 396 ± 11 s in the presence of 0.25 mM (**Figure 2f, Table S1**).

Since GUV fusion is reported to be dependent on environmental factors, we also studied the role of temperature and lipid composition on fusion efficacy. Lipid mixing induced by TX-100 was more efficient as the solution temperature increased from 21°C to 37°C, as demonstrated by a 20 % increase in peak RatioA at the CMC (**Figure 2g**). As the solution temperature reduced below 21°C, reflecting a move towards the lipid gel-phase, the concentration requirements to achieve maximum fusion increased ~6-fold, and the peak FRET efficiency returned to values comparable to those measured at 21°C. While the increased concentration requirements to achieve fusion may reflect variations in TX-100 micelle size and hydration[36], the increased peak FRET efficiency observed at 37°C likely indicates an abundance of fused vesicle states. Regarding lipid composition, previous studies indicated that cholesterol modulates TX-100 induced expansion and solubilization[18], however here we observed little change in the observed FRET efficiency magnitudes when both POPC and POPC-POPS LUVs contained modest concentrations (0 – 30%) of cholesterol (**Figures S8** and **S9**). That said, the concentration requirements to achieve fusion decreased by ~0.2 mM when vesicles composed of DMPC and DPPC lipids were used (**Figure S10**). Although further work is required to disentangle the influence of vesicle porosity, roughness, and lipid charge, the degree of lipid mixing doubled in such cases, indicating that the lipid composition itself plays a key role in modulating fusion efficacy.

To further characterize the interaction and assess the degree of solution exchange between fusing vesicles, we also implemented an approach whereby vesicles encapsulating the fluorescent calcium indicator Cal-520 were fused with vesicles encapsulating Ca^{2+}. This approach is similar in nature to other content mixing assays where changes in fluorescence intensity of the content is observed upon solution exchange between fusing vesicles[37]. While Cal-520, the fluorescence intensity of which increases upon Ca^{2+} binding, has been used to assess vesicle permeabilization in response to disruptive proteins and other non-ionic detergents[29, 38], we quantified the magnitude of Ca^{2+} flux between adjoining vesicles, as illustrated in **Figure S11**. In this case, Ca^{2+} entry into vesicles encapsulating Cal-520 triggers a local Ca^{2+} concentration increase, providing a concentration-dependent enhancement of Cal-520 intensity at ~520 nm. Prior to experimentation, nonencapsulated molecules were removed by size exclusion chromatography as detailed in the Methods. As TX-100 was progressively titrated at 21°C into a 1: 1 mixture of Cal-520: Ca^{2+} loaded vesicles, a 2.5-fold increase in Cal-520 emission intensity was observed (**Figure S11**) at fusion-inducing detergent concentrations. Control experiments performed independently on free Cal-520 in solution indicated that the dye's fluorescence response is insensitive to TX-100, and that it responds to Ca^{2+} in detergent-rich media (**Figure S12**), providing confidence that encapsulated cargo can be transported between vesicles during the fusion process. We note that the Cal-520 intensity remained largely unchanged at solubilizing detergent concentrations above 0.3 mM. Although Cal-520 shares a comparable calcium affinity (k_d = 345 nM) with earlier generation dyes such as Fluo-3 (k_d = 325 nm) and Fluo-4 (k_d = 345 nm), its binding specificity has been enhanced[39]. While such parameters likely depend on the solution environment (temperature, pH), the lack of variation in the binding curve at high TX-100 concentrations likely reflects strong affinity between the dye and $Ca2^{+}$ as the vesicles transition from the fused to solubilized state. A Hill model[18] applied to the data shown in **Figure S11** also revealed a half-maximal concentration constant (0.17 ± 0.02 mM) below the CMC. When compared with the FRET measurements shown in **Figure 2d**, which indicate substantial levels of lipid mixing at comparable TX-100 concentrations, the implication is that combinations of membrane permeabilization and content exchange occur concurrently with fusion events in the ensemble. While previous results suggest that Ca^{2+} itself induces fusion between negatively charged vesicles[40, 41], we previously identified that Ca^{2+} has minimal influence on POPC vesicle fusion[29], giving further assurance that the observed Cal-520 spectral enhancements are due to TX-100 induced fusion.

The Fusion Mechanism involves Docking, Hemifusion and Full Lipid Mixing

To further explore the observed structural changes, and to dissect the mechanism of fusion, we next performed single-vesicle imaging via a custom-built wide-field objective-type total internal reflection fluorescence microscope that enables the simultaneous imaging of DiI and DiD emission[42]. Here, POPC vesicles incorporating 2 % DiI were induced to fuse with LUVs incorporating 2 % DiD and 1 % biotin-PE such that fused species could be tethered to a glass coverslip functionalized with biotinylated BSA and NeutrAvidin (**Figure 3a**). Vesicles were added to a surface-functionalized coverslip after incubation with TX-100, and DiI and DiD fluorescence trajectories were collected with 50 ms time integration. Fused vesicles were then identified by the appearance of co-localized diffraction limited spots across both detection channels (**Figure 3b**) and lipid mixing between vesicles was observed via an appearance or enhancement in the mean FRET efficiency per vesicle. In the presence of 0 – 0.2 mM TX-100, the traces obtained from > 500 individual FRET-active species were photostable over the duration of the measurement (**Figure 3c, Figure S13)** and the population distributions of FRET efficiencies showed a major peak at ~0.1 (**Figure 3d**), suggestive of close contact or docking between DiI and DiD-labelled vesicles, but without substantial lipid mixing. As the TX-100 concentration then increased towards 0.5 mM, the low FRET population decreased in favour of a broad distribution of high FRET states that reached a value of 0.7

at 0.5 mM, suggestive of substantial lipid mixing events (**Figure 3d**). We note the observed shift in the distributions from low to high FRET efficiencies broadly reflect the changes observed in the ensemble and the observation of FRET states between 0.1 and 0.7 reflect the morphological heterogeneity of intermediates that are structurally different from the fully fused state in which both leaflets have fully mixed. We therefore assigned E_{FRET} = 0.7 as an indicator of full fusion, in which both leaflets of the vesicle fully mixed, whereas intermediate states were assigned to hemi-fusion, where only partial lipid mixing was achieved. In all cases, tri-Gaussian functions were fitted to the FRET efficiency histograms, and used to identify thresholds of $E_{FRET} < 0.25$, $0.25 \geq E_{FRET} \leq 0.55$ and $E_{FRET} > 0.55$ for classification of docked, hemi-fused and fully-fused species respectively. As shown in **Figure 3e**, the percentage of species exhibiting full fusion increased 5-fold across the titration, whereas the number of docked species progressively diminished. Overall, the imaging of single fused species via FRET confirmed the presence of intermediate states along the fusion process, with each state characterized by discrete values of FRET efficiency and thus DiI-DiD separation distance.

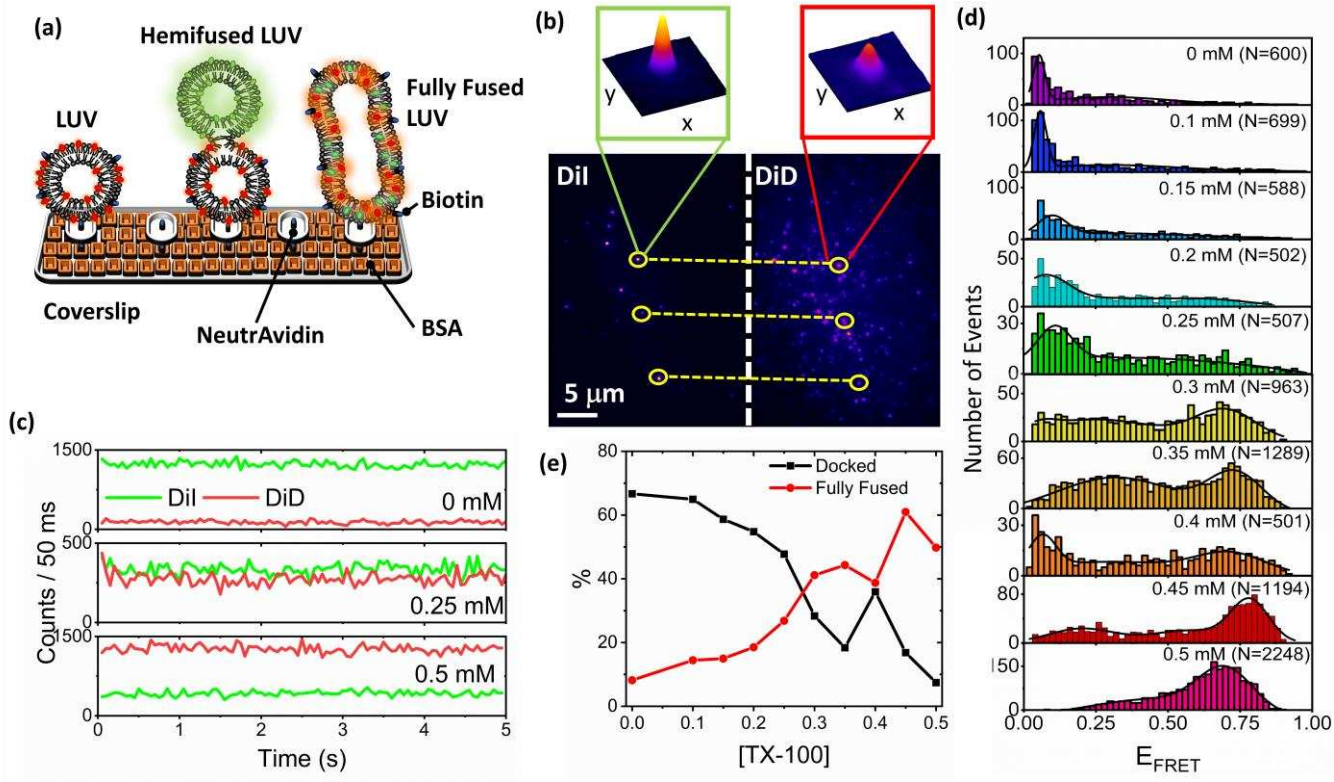

Figure 3. TX-100 induces vesicle docking, hemifusion and full lipid mixing. (a) Schematic illustration of the immobilization scheme. LUVs incorporating 2 % DiD and 1 % Biotin-PE were fused with LUVs incorporating 2 % DiI and attached to a coverslip via BSA, biotin and NeutrAvidin. (b) Representative TIRF image obtained from surface-tethered LUVs in the presence of TX-100, showing co-localized DiI and DiD regions (yellow circles) (λ_{ex} = 532 nm). Insets: 3D intensity profiles of DiI and DiD emission obtained from a single fusion product. (c) Representative DiI (green) and DiD (red) intensity traces obtained from individually fused LUVs in the absence and presence of TX-100. (d) Histograms of the mean apparent FRET efficiency obtained from N > 500 surface immobilized vesicles before and after incubation with TX-100 rich solutions. Solid black lines represent tri-Gaussian fits. (e) Variation in the number of docked ($E_{FRET} < 0.25$) versus fully fused ($E_{FRET} > 0.55$) species observed as a function of TX-100.

To further confirm the presence of multiple intermediates, we also acquired scanning electron microscopy (SEM) micrographs of vesicles in the absence and presence of fusion-promoting detergent concentrations. Without TX-100, the vesicles (N = 242) were predominantly spherical, exhibiting a mean circularity, ϕ, of 0.84 ± 0.15, and a mean particle size, d, of 246 ± 61 nm, with little evidence of fusion (**Figure 4a, Figure 4f,**

Figure S14). Upon incubation with TX-100, the mean particle size then increased 2-fold (d = 528 ± 56), the majority of species were elliptical (ϕ = 0.62 ± 0.22) (**Figure 4f)** and four major species were identified. First, we observed adjoined vesicles without evidence of clefting, which we interpreted as early fusion products that involve vesicle docking (**Figure 4b, Figure S15**). Further examination revealed vesicles within close proximity but with a clear cleft between adjacent surfaces (**Figure 4c, Figure S16**). Based on the similarity of these structures to those observed in previous studies of protein-induced vesicle fusion[43, 44], we assigned these events to intermediate hemi-fusion products involving two or more vesicles. Finally, we observed the appearance of much larger micron-sized ellipses **(Figure 4d, Figure S17**) and larger conglomerates (**Figure 4e, Figure S18**) which we interpreted as evidence of multiple fusion events. Closer inspection of the surface topography of such species also indicated variations in texture, protrusions and indentations which we speculate could be indicative of pore formation and/or dissociation of membrane regions (**Figure 4c**)**.**

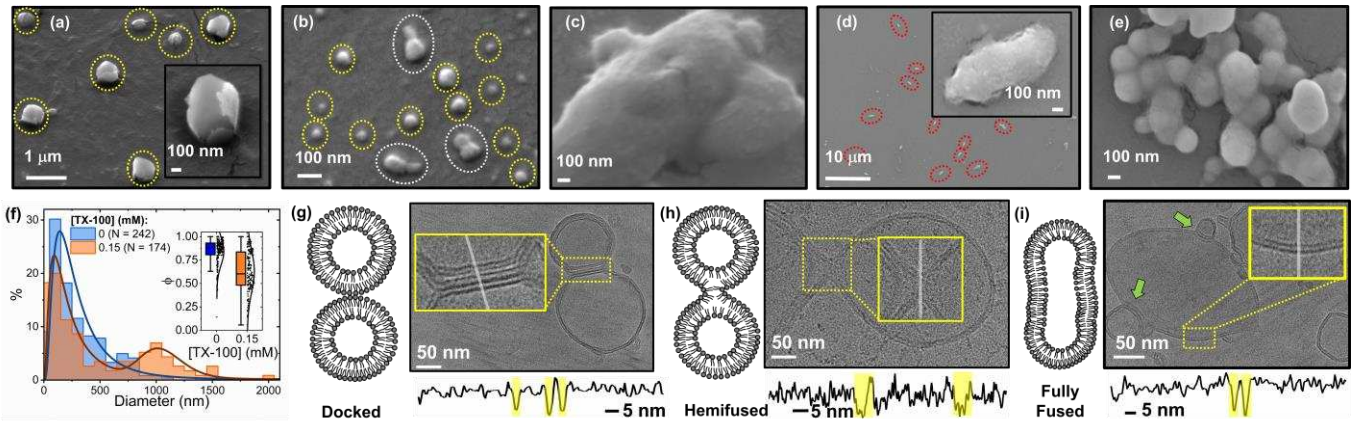

Figure 4. Confirmation of fused vesicles by SEM and Cryo-TEM. (a) SEM micrographs of in-tact vesicles in the absence and (b-e) presence of 0.15 mM TX-100 showing intact immobilized vesicles (yellow dashed regions), docked vesicles (white dashed regions), and large elliptical species (red dashed regions) assigned to full fusion. (f) Size distribution histograms obtained from vesicles in the absence (blue) and presence (orange) of 0.15 mM TX-100. Inset: comparative bar plot summarizing the corresponding variation in particle circularity. (g) Schematic (left panel) and representative cryo-TEM image (right panel) of docked, (h) hemi-fused and (i) fully fused species. Insets: regions of interest at higher magnification showing bilayers defined by the luminal grey level distribution (bottom panels). The green arrows indicate further docking or budding events.

Having demonstrated TX-100 induced morphological changes by SEM, we next used Cryo-TEM to visualize interactions between adjacent membranes. Here, the majority of isolated vesicles were in-tact and unilamellar (**Figure S19**). In agreement with previous observations[45], we also identified lower populations (< 40 %) of vesicles containing multiple bilayers (**Figure S20**). Based on the prior FRET and SEM analysis, and in line with models predicted for extracellular vesicle fusion[46], we hypothesized that TX-100 induced fusion intermediates consist of (i) docked vesicles showing close contact between the lipid bilayers, but without lipid mixing, (ii) progressive fusion of the outer and inner leaflets leading to a fusion pore and content exchange and (iii) development of the fused pore into a fully fused state where both leaflets had fully mixed. Indeed, we identified examples of where the membranes of opposing vesicles were in parallel and within close proximity (< 5 nm), but with a clear barrier separating the vesicle interiors (**Figure 4g**). We also identified structures where the bilayer leaflets had merged at a ~25 nm diameter contact pore, and where the two bilayers transitioned continuously from one vesicle to the other (**Figure 4h**). The fully fused species, after expansion of the fusion pore and upon complete content mixing, was then captured as a larger fusion product containing a single bilayer, with no evidence of a barrier preventing content mixing (**Figure 4i**). In some cases, we also observed examples of where further vesicles had either docked

to or budded from the fully fused form (**Figure 4i**). While the current Cryo TEM analysis cannot differentiate between further docking or budding events, we note that TX-100 has been shown to induce vesicle budding in GUVs of similar composition[47, 48, 49], and the release of smaller species. Nevertheless, these results further demonstrate the multi-step nature of the TX-100 induced vesicle fusion process.

TX-100 Enables Vesicle Fusion to Solid Surfaces

Controllable vesicle fusion to surfaces has vast potential for a range of applications including biosensing and drug delivery[50]. We therefore explored whether TX-100 could controllably fuse vesicles in solution with vesicles pre-immobilized on a solid surface, allowing for real-time content delivery and solution exchange. Here, we assessed the kinetics of accumulated mass transfer and variations in surface viscoelasticity via a quartz crystal microbalance with dissipation monitoring approach. POPC vesicles incorporating 1 % biotin-PE were first tethered to a bovine serum album coated SiO_2 substrate incorporating 2 % biotin via NeutrAvidin as described in **Figure 3a**. The frequency and dissipation signals, reflecting surface mass and viscoelasticity, respectively, were then recorded under equilibrium and exposure to a constant flow rate. **Figure S21** shows representative QCM-D kinetics recorded upon injection of BSA-Biotin, Neutravidin and biotinylated vesicles. After the sensors were saturated with vesicles, the surface was washed with 50 mM Tris (pH 8) buffer to remove unattached species. Importantly, the frequency and dissipation responses from the sensor showed little recover after the wash step indicating successful surface tethering. Next, vesicles lacking biotin-PE at a final lipid concentration of 0.16 mg/mL were flushed across the sensor surface in the absence and presence of TX-100. Negligible vesicle deposition was noted in the absence of TX-100, indicated by the lack of variation in both the frequency and dissipation responses (**Figure S21**). When a solution containing LUVs and 0.1 mM TX-100 was injected across the layer, an initial 20 Hz reduction in frequency, concurrent with a 1.2-fold increase in dissipation was recorded, indicative of (i) a mass gain over the period of the injection lasting tens of minutes and (ii) structural rearrangements on the surface (**Figure 5a**). We assigned the bi-exponential nature of the frequency decay to combinations of detergent interactions with the immobilized layer and vesicle-vesicle interactions on the surface. Experiments performed independently to assess the interaction between freely-diffusing TX-100 with surface-tethered vesicles indicated only a 4-5 Hz shift upon injection (**Figure S22**) [18], suggesting that the observed frequency change shown in **Figure 5a** is mostly due to TX-100 induced vesicle-vesicle interactions on the surface. When the concentration of TX-100 was doubled, similar rate constants were observed (334 ± 4 s^{-1}) for the frequency decay though we note that the magnitude of the relative frequency and dissipation responses increased 1.5- and 2.5-fold respectively pointing towards an abundance of fused states on the surface (**Figure 5b**). When both surfaces were washed with solution, only a partial recovery in ΔF and ΔD was observed indicating that most of the deposited material irreversibly attached to the immobilized layer (**Figures 5a and 5b**). However, when detergent concentrations above the CMC were in the injectant, the deposited mass returned towards the initial frequency and dissipation levels during the wash step, suggesting rupture of the freely-diffusing vesicles upon interaction with the surface, and the subsequent removal of lipid mass (**Figure 5c**). Indeed, these assertions were further confirmed when variations in frequency were plotted against dissipation across the timescale of the fusion interaction (**Figure S23**). The slope of the dissipation changes versus frequency shown in **Figure S23** reflect variations in the viscoelastic properties of the immobilized layer across time. For detergent concentrations below the CMC, these changes broadly indicate that mass gain coupled with viscoelasticity enhancements on the surface precede minor levels of mass loss upon washing. At concentrations above the CMC, the vesicles in solution are susceptible to lysis and dissociation: a finding that we note is in line with our previous ensemble FRET approaches.

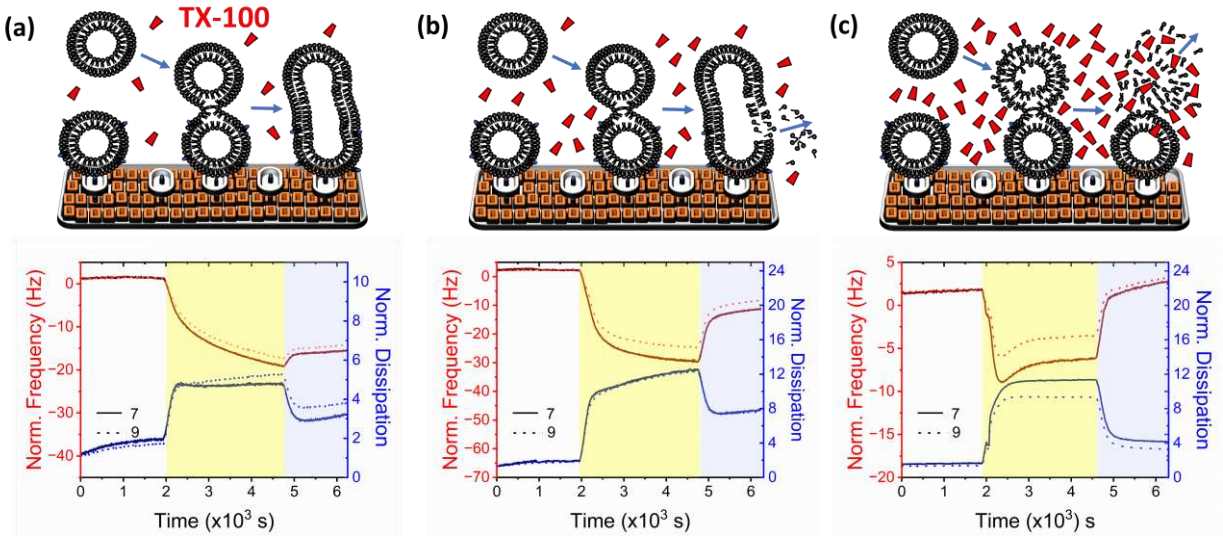

Figure 5. QCM-D analysis of TX-100 induced vesicle fusion on solid surfaces. Normalized variation in frequency (red) and dissipation (blue) associated with the 7th (solid lines) and 9th (dashed lines) harmonics upon injection of LUVs and (a) 0.1 mM, (b) 0.2 mM and (c) 0.3 mM TX-100 to a surface functionalized with BSA-biotin, NeutrAvidin and biotinylated LUVs. Injection of TX-100 and freely-diffusing LUVs is denoted by the yellow shaded area and was performed after washing the vesicle saturated surface with 50 mM Tris buffer (pH 8). The blue shaded area corresponds to the final wash step when post-interaction, the surface was rinsed with buffer. The cartoons (top panels) illustrate the lipid phases (docked, hemifused, fully fused and lysed) on the surface as the experiment proceeds.

Discussion

Several studies provide support for the hypothesis that TX-100 induces fusion of sub-micron sized vesicles. For instance, optical microscopy experiments have almost exclusively demonstrated GUV fusion to fluorescently-tagged native membranes at sub-solubilizing TX-100 concentrations[22] and similar approaches have been employed to achieve TX-100-induced fusion between proteoliposomes and native membranes, resulting in the reconstitution of transmembrane proteins into GUVs[7, 8, 23]. In confocal-based fluorescence experiments, fusion was observed between permeable GUVs, suggestive that the process can occur through an initial contact between pores on adjoining vesicles[15]. However, these assays, while informative, cannot dissect the multi-step mechanism of membrane fusion at the higher end of the membrane curvature space.

To overcome this challenge, we implemented a robust in vitro fusion assay based on the measurement of energy transfer between lipophilic membrane dyes during lipid mixing. Supported by a range of ensemble and single-particle measurements, we demonstrate that the assay unveils multiple fusion intermediates as recorded by stepwise changes in the FRET efficiency. Furthermore, the fusion process can be readily visualized by SEM and Cryo-TEM, both of which provide information on the morphology of the intermediates and their occurrence under varying TX-100 conditions. By leveraging these benefits, we identified that TX-100 induced fusion of highly curved LUVs in vitro is unidirectional, precedes solubilization, and occurs via a mechanism that involves vesicle docking, hemifusion, content exchange and full lipid mixing. This is striking for two reasons: first, the fusion process occurs at sub-solubilizing detergent concentrations below the CMC and second, the fusion products observed here are remarkably similar to those observed during protein-induced vesicle fusion and viral fusion, raising the tantalising possibility that the observed intermediates are common, and share structural similarities, regardless of

the fusogen. Moreover, we provide evidence that the fusion efficacy is modulated by local environmental factors including temperature and lipid composition, and this work now opens a platform for exploring a matrix of variables that may regulate the interaction.

Remarkably, our QCM-D results also show discrete steps of vesicle fusion and serve to highlight the benefits of using TX-100 to controllably fuse vesicles to surfaces: an important observation that may find direct relevance in a wide range of biotechnological applications. For example, in targeted drug delivery, vesicles encapsulating therapeutic agents are required to fuse to target sites, controllably releasing the encapsulated molecule. Vesicle fusion to surfaces can also be employed to create biomimetic systems that mimic natural cellular structures, or controllably modify and functionalize materials for enhancement of properties including conductivity and chemical reactivity. There is also scope for the fusion products to be used or manipulated in the context of sensor development, for instance in the detection of specific analytes, or in microfluidic devices where vesicle fusion can be employed to create well-defined membrane structures or facilitate the controllable transport and manipulation of small liquid volumes. We previously suggested that TX-100, along with other non-ionic surfactants induce swelling of lipid vesicles, but the absence of fusion observed with detergents such as Tween-20, suggest that the fusion efficacy is detergent-dependent (**Figure S24**). Nevertheless, we expect the presented tools and techniques will be used to further define the fusion mechanism when different vesicle subpopulations are introduced, and to disentangle the impact of vesicle curvature, presence of lipid rafts and other environmental factors (pH, ionic strength) which may regulate the interaction. Indeed, the combined approaches and developed tools unambiguously dissect the underlying mechanism of TX-100-induced vesicle fusion and could become an indispensable toolbox for further characterizing the influence of fusogens, including those with important biomedical significance. Moreover, dissecting the mechanism of LUV fusion is critical, not only for expanding our fundamental knowledge of vesicle biology, but for the development of biocompatible and tissue-specific delivery systems.

A major aspect of our results that deserves attention is that sub-solubilizing concentrations of TX-100 were required to produce the fusion states described. This not only implies that individual TX-100 monomers play a key role in initiating vesicle fusion, but is particularly remarkable because non-ionic detergents typically achieve structural changes only once above their CMCs. While further work is required to elucidate the precise role of the molecule in initiating fusion, we hypothesise that sufficiently high local detergent densities on the membrane may act as a nucleation site for docking, potentially via a pathway that involves creation of pores. Our approaches enabled fusion intermediates to be observed up to detergent: lipid ratios of ~ 5: 1, suggesting that morphological rearrangements and solution exchange are initiated during LUV-detergent saturation. While membrane saturation and insertion of TX-100 into the bilayer may lead to local invaginations and permeabilization within in-tact vesicles prior to fusion, it's possible that bilayer bending due to vesicle swelling could also facilitate the process. It is also worth re-emphasizing a key benefit of the FRET-based strategy: unlike conventional phase contrast or fluorescence-based imaging, where only a 2-dimensional plane is captured, the FRET response reports on the dye separation distance across the entire 3-dimensional volume of the fused species.

Conclusions

The approaches described here provide a general framework for dissecting the precise molecular level events that lead to TX-100 induced LUV fusion in vitro. TX-100 dynamically alters the conformation and integrity of both freely-diffusing and surface-immobilized vesicles via a mechanism involving vesicle

docking, hemifusion, content exchange and full lipid mixing, prior to solubilization and lysis. These observations provide new mechanistic insights for how the widely used TX-100 detergent dynamically perturbs and modulates highly curved membrane structures, even at concentrations below the CMC. We anticipate that our current demonstration will be a starting point for addressing many important aspects of vesicle fusion, and may be directly relevant to key biotechnological applications where targeted vesicle fusion, especially to surfaces, is critical. We also expect that the developed approaches will find general utility for unveiling the multi-step mechanism of vesicle fusion in response to additional perturbative agents, including membrane-disrupting proteins and anti-viral agents, and could have important implications for evaluating drug delivery efficiencies.

Methods

Materials

POPC, 1-oleoyl-2-(12-biotinyl(aminododecanoyl))-sn-glycero-3-phosphoethanolamine (biotin-PE), 1-palmitoyl-2-oleoyl-sn-glycero-3-phospho-L-serine (POPS), 1,2-dipalmitoyl-sn-glycero-3-phosphocholine (DPPC) and 1,2-dimyristoyl-sn-glycero-3-phosphocholine (DMPC) lipids in chloroform were purchased from Avanti Polar Lipids and used without additional purification. Cholesterol was purchased from Sigma Aldrich and dissolved in chloroform prior to use. TX-100 was purchased from Sigma Aldrich and freshly suspended in 50 mM Tris buffer (pH 8) prior to each use. 1,1'-Dioctadecyl-3,3,3',3'-Tetramethylindocarbocyanine (DiI) and 1,1'-Dioctadecyl-3,3,3',3'-Tetramethylindodicarbocyanine (DiD)) were purchased from ThermoFisher Scientific and used without additional purification. All lipid and cholesterol stock solutions were stored in chloroform at -20^{o}C prior to use, whereas DiI and DiD stock solutions from the manufacturer were stored at 4^{o}C.

Preparation of vesicles incorporating DiI and DiD

Large unilamellar vesicles composed of lipid, cholesterol, biotin-PE and either DiI or DiD were prepared immediately prior to each experiment by extrusion. Briefly, unlabelled lipids and fluorescently labelled lipids were mixed in chloroform at the ratios specified in the main text prior to evaporation of the solvent by application of a gentle nitrogen stream. The resulting lipid film was resuspended in 50 mM Tris buffer (pH 8) and mixed well by vortex. Final solutions were then extruded through a polycarbonate membrane filter with size cut off of 200 nm prior to use.

Preparation and purification of vesicles encapsulating Cal-520 and Ca^{2+}

Vesicles encapsulating either Cal-520 or Ca^{2+} were prepared as previously described[29]. Briefly, chloroform was removed from POPC lipid stocks under gentle nitrogen flow, and the resulting thin lipid film was dissolved and vortexed in 50 mM Tris buffer (pH 8) containing either 100 mM Cal-520 or 10 mM Ca^{2+}. The solutions were then extruded at least 21 times through a 200 nm cut off polycarbonate membrane filter (Avanti Polar Lipids). Vesicles were then filtered using PD-10 desalting columns (Sigma Aldrich) to separate non-encapsulated molecules from the loaded vesicles.

Isothermal Titration Calorimetry

Isothermal titration calorimetry was performed using a Malvern MicroCal VP-ITC system (Malvern Panalytical). All TX-100 and vesicle solutions were degassed under vacuum prior to use. Briefly, POPC vesicles were placed in a calorimetric cell at a final lipid concentration of 88 μM (50 mM Tris, pH 8), and 5 mM TX-100 was injected in 2-10 μL steps (3.5-minute intervals) at a rate of 2 s/μL. The vesicles were continuously stirred at 290 rpm throughout the measurement. Similar experiments were also performed involving the titration of TX-100 directly into buffer solution. Reaction heats were then calculated by integration of the peaks of each injection.

Steady State FRET Vesicle Fusion Assay

200nm sized POPC vesicles incorporating 2 % DiI were suspended in 50 mM Tris buffer (pH 8) with those incorporating 2 % DiD at a DiI-LUV: DiD-LUV ratio of 1: 3 and final lipid concentration of 88 μM. The solution was then gently stirred by magnetic stirring at 1.5 Hz. Fluorescence emission spectra were then acquired using a HORIBA Fluoromax-4 spectrophotometer with excitation wavelengths of 520 nm and 620 nm. All emission spectra were corrected for background and acquired under magic angle conditions. Apparent FRET efficiencies were estimated via $E_{FRET} = I_A/(I_A+I_D)$ where I_D and I_A represent the integrated fluorescence emission intensities of DiI and DiD, respectively. We also measured the efficiency of energy transfer using the RatioA method which yields a value proportional to E by comparing the magnitude of sensitized acceptor emission to the emission obtained under direct excitation of the acceptor. Plots of E versus [TX-100] are reported as the mean and standard error from three experimental runs.

Time Correlated Single Photon Counting

Time-resolved fluorescence decays were acquired using a FluoTime 300 instrument equipped with a pulsed 530 nm excitation line (80 MHz) and PMA Hybrid 07 photomultiplier tube (Picoquant). Briefly, DiI and DiD loaded POPC vesicles were mixed as described previously and magnetically stirred at 1.5 Hz. Fluorescence lifetime decays at an emission wavelength of 565 nm were then collected under magic angle conditions until 10^4 photon counts accumulated at the decay maximum. Decay curves were then fitted by iterative reconvolution of the instrument response function and the observed intensity decay, I_t, using a multi-exponential decay of the form $\boldsymbol{I_t = \sum_{i=1}^{n} a_i e^{-\frac{t}{\tau_i}}}$, a_i and t_i represent the fractional amplitudes and lifetimes of the i'th decay components. All experiments were performed in 50 mM Tris buffer (pH 8) using DiI-LUV: DiD-LUV ratios as specified in the main text and final lipid concentrations of 88 μM.

Dynamic Light Scattering

Hydrodynamic radii of vesicles in TX-100-rich solutions were estimated using a Zetasizer mV DLS system (Malvern Panalytical) equipped with a 632.8 nm laser line. Briefly, POPC LUVs at a final lipid concentration of 88 μM were suspended in 50 mM Tris buffer (pH 8, n = 1.33) and TX-100 was added at the desired concentration. Correlation functions, g(τ), produced via the intensity of scattered light were fitted to a single-species model of the form $g(\tau) = \beta(e^{-\Gamma\tau}\left[1+\frac{1}{2}\mu_2\tau^2\right])^2$ or a multi-species model of the form $g(\tau) = \sum_n\left(\beta_n(e^{-\Gamma_n\tau})\right)^2$, where β is the coherence factor, μ is the central moment of the distribution of decay rates and Γ is the decay rate . Diffusion times, τ, where then related to the diffusion coefficients, D, via $\Gamma=Dq^2$, where q is the wave factor. Hydrodynamic radii were then extracted using the Stokes-Einstein equation as discussed elsewhere[51]. All DLS measurements were performed using 178° backscattering, and

intensity-size distributions were fitted to a lognormal distribution of the form $I = y_0 + \frac{A}{\sqrt{2\pi}wx} e^{-\frac{\left[\ln\left(\frac{x}{x_c}\right)\right]^2}{2w^2}}$, where y_0 is the offset, x_c is the centre of the distribution, w is the log standard deviation and A is the area.

Fluorescence Correlation Spectroscopy

FCS experiments were performed using a Zeiss LSM 880 microscope equipped with a 514 nm excitation line and GaAsP detector. LUVs incorporating 99 % POPC and 0.1 % DiI were diluted in 50 mM Tris buffer (pH 8) to a final lipid concentration of 6 μM, pipetted onto a pre-cleaned microscope slide, and sandwiched to a 1.5 glass coverslip via silica. Typical excitation powers were 4 μW as measured at the sample plane. Correlation curves were fitted to an equation of the form $\boldsymbol{G(\tau) = y_0 + \frac{1}{n}\frac{1}{(1+\tau/\tau_{\text{diff}})}\frac{1}{\sqrt{1+\tau/SP^2\tau_{\text{diff}}}}\left(1 + \frac{Te^{\tau/\tau_{\text{trip}}}}{1-T}\right)}$ where y_0, n, τ, $\boldsymbol{\tau_{\text{diff}}}$, SP, T and $\boldsymbol{\tau_{\text{trip}}}$ are the offset, effective number of particles in the confocal volume, lag time, residence time in the confocal volume, structure parameter (which describes the shape of the detection volume and is equal to $\boldsymbol{\omega_{xy}/\omega_z}$ where ω is the width of the laser spot in the x, y and z directions), fraction of particles in the triplet state and residence time in triplet state, respectively. Diffusion coefficients were then determined as described previously and the hydrodynamic radius was estimated via the Stokes-Einstein relationship.

Quartz Crystal Microbalance with Dissipation Monitoring

QCM-D experiments were performed using a Q-Sense E4 system (Biolin Scientific) instrument. Briefly, SiO_2 coated substrates (Biolin Scientific) with a fundemantal frequency of 5 MHz were first cleaned by UV ozone for 10 minutes, then sonicated in 2 % Hellmanex III for 10 minutes and ultrapure Milli-Q water for 20 minutes. The sensors were then dried under nitrogen before being treated with UV ozone for an additional 30 minutes. The sensors were then immersed in 4 % v/v ATES/IPA solution for 16 hours to produce an amine monolayer and dried under nitrogen before being installed in the sensor housing module. All sensors were washed with 50 mM Tris (pH 8) under a flow rate of 20 μL/min until a stable baseline, defined as < 5 Hz shift / minute was achieved. At the start of each experiment, the sensor surfaces were washed sequentially with 0.1 mg/mL biotinylated bovine serum albumin (BSA), 1 mg/mL BSA and 0.2 mg/mL NeutrAvidin. Between each addition, the sensors were washed with buffer to remove any unbound molecules. Vesicles incorporating 1 % Biotin-PE were then flushed across the surface at a final lipid concentration of 0.25 mg/mL until saturation of the surface was reached, followed by another buffer wash step. Next, POPC vesicles lacking Biotin-PE at a final lipid concentration of 0.16 mg/mL were mixed with TX-100 at the specified concentrations and immediately washed over the sensor surface.

Single Vesicle FRET Spectroscopy

Microfluidic flow cells were constructed as previously described[42] and coated with 0.1 mg/mL BSA-Biotin, 1 mg/mL BSA and 0.2 mg/mL NeutrAvidin. Biotinylated POPC vesicles incorporating 2 % DiD were mixed with non-biotinylated vesicles containing 2 % DiI (DiI-vesicle: DiD vesicle = 1: 3) at a final lipid concentration of 88 μM in TX-100 rich media (50 mM Tris buffer, pH 8) prior to addition to the functionalized surface. Unbound vesicles were then removed by washing the flowcell with buffer. Objective-based TIRF microscopy was then performed on an inverted Nikon Eclipse Ti microscopy containing a 100 x NA 1.49 oil immersion objective lens (Nikon)[42]. Excitation was achieved from a continuous wave 532 nm laser line

(Obis, Coherent) with the diameter of the illuminated region in the field of view calculated to be 26 μm. DiI and DiD emission was spatially separated using a DualView Image Splitter (Photometrics) containing a dichroic (T640LPXR, Chroma) and band pass filters (ET585/65M and ET700/75M, Chroma) and imaged in parallel on a back-illuminated Prime 95b CMOS camera cooled to -30ºC (Photometrics). Fluorescence and FRET trajectories from immobilized vesicles were acquired with 50 ms exposure time and recorded images were analysed in MATLAB (R2019a) using iSMS FRET microscopy software[52]. Briefly, co-localized DiI and DiD emission trajectories, termed I_D and I_A respectively, were obtained by integration of the intensity within the area containing the vesicle of interest at each time point, and apparent FRET efficiencies, E_{FRET}, were estimated as previously described.

Scanning Electron Microscopy

SEM images were acquired using a JEOL JSM 7800-F system operating at 5kV. Vesicles were induced to fuse in 50 mM Tris (pH 8) conditions containing TX-100 as specified in the main text, diluted and deposited onto a silicon substrate. The solution was then evaporated and the immobilized vesicle layer was sputtered with a 5 nm layer of Pt/Pd. We note that the final concentration of vesicles applied to the substrate was sub-nM to prevent the formation of conglomerates that are not directly correlated to the effects of TX-100. This was confirmed by the fact that for low TX-100 concentrations, and for vesicles imaged in the absence of detergent, we did not observe any vesicle clusters. Vesicle diameters were determined using ImageJ, where automated analysis of black and white binary images enabled separation of regions of white pixels (vesicles) against a dark background. Vesicle circularity was measured via $4p(A/p^2)$, where A is the 2-dimensional surface area of the vesicle and p is the vesicle perimeter.

Cryo-TEM

Cryo-TEM was used to directly visualize fused vesicle species using a procedure described elsewhere[45]. Briefly, Quantifoil copper R 1.2/1.3 200 mesh grids (Electron Microscopy Sciences) were prepared by glow discharging at 20 mA and 0.26 mbar for 1 minute in a Pelco easiGlow glow discharge system. Small volumes of vesicles pre-incubated with TX-100 were than applied to the carbon side of the EM grid in 90 % humidity. Excess liquid was blotted off and the grids were plunge frozen into precooled liquid ethane using a Vitrobot system (Thermo Scientific), allowing fused species to be embedded and preserved within a thin layer of amorphous ice. Micrographs were then obtained using a Thermo Scientific Glacios Cryo-TEM microscope using an operating voltage of 200 kV and 120,000x magnification.

Acknowledgements

This work was supported by Alzheimer's Research UK (RF2019-A-001) and EPSRC (EP/P030017/1, EP/W024063/1). We thank Prof. Daniella Barillá (Department of Biology, University of York) for use of DLS instrumentation, Dr. Jamie Blaza (Department of Biology, University of York) for technical expertise and use of Cryo-TEM, Dr. Laura A. Clark (School of Physics, Engineering and Technology, University of York) for advice related to EM image analysis, and Prof. Thomas Krauss (University of York) for use of SEM facilities. We also thank the Bioscience Technology Facility (University of York) for use of ITC, FCS and fluorescence spectroscopy facilities, and Dr Laurence Wilson (University of York) for critically reading the manuscript.

References

1. Gennuso F, Fernetti C, Tirolo C, Testa N, L'Episcopo F, Caniglia S*, et al.* Bilirubin protects astrocytes from its own toxicity by inducing up-regulation and translocation of

multidrug resistance-associated protein 1 (Mrp1). *Proc Natl Acad Sci U S A* 2004, **101**(8)**:** 2470-2475.

2. Rajagopal A, Pant AC, Simon SM, Chen Y. In vivo analysis of human multidrug resistance protein 1 (MRP1) activity using transient expression of fluorescently tagged MRP1. *Cancer Res* 2002, **62**(2)**:** 391-396.

3. Koley D, Bard AJ. Triton X-100 concentration effects on membrane permeability of a single HeLa cell by scanning electrochemical microscopy (SECM). *Proc Natl Acad Sci U S A* 2010, **107**(39)**:** 16783-16787.

4. Ishkhanyan H, Rhys NH, Barlow DJ, Lawrence MJ, Lorenz CD. Impact of drug aggregation on the structural and dynamic properties of Triton X-100 micelles. *Nanoscale* 2022, **14**(14)**:** 5392-5403.

5. Welch SR, Davies KA, Buczkowski H, Hettiarachchi N, Green N, Arnold U*, et al.* Analysis of Inactivation of SARS-CoV-2 by Specimen Transport Media, Nucleic Acid Extraction Reagents, Detergents, and Fixatives. *J Clin Microbiol* 2020, **58**(11).

6. Colavita F, Quartu S, Lalle E, Bordi L, Lapa D, Meschi S*, et al.* Evaluation of the inactivation effect of Triton X-100 on Ebola virus infectivity. *J Clin Virol* 2017, **86:** 27-30.

7. Kragh-Hansen U, le Maire M, Moller JV. The mechanism of detergent solubilization of liposomes and protein-containing membranes. *Biophys J* 1998, **75**(6)**:** 2932-2946.

8. Urbaneja MA, Goni FM, Alonso A. Structural changes induced by Triton X-100 on sonicated phosphatidylcholine liposomes. *Eur J Biochem* 1988, **173**(3)**:** 585-588.

9. Paternostre MT, Roux M, Rigaud JL. Mechanisms of membrane protein insertion into liposomes during reconstitution procedures involving the use of detergents. 1. Solubilization of large unilamellar liposomes (prepared by reverse-phase evaporation) by triton X-100, octyl glucoside, and sodium cholate. *Biochemistry* 1988, **27**(8)**:** 2668-2677.

10. Lete MG, Monasterio BG, Collado MI, Medina M, Sot J, Alonso A*, et al.* Fast and slow biomembrane solubilizing detergents: Insights into their mechanism of action. *Colloid Surface B* 2019, **183**.

11. Clark ST, Arras MML, Sarles SA, Frymier PD. Lipid shape determination of detergent solubilization in mixed-lipid liposomes. *Colloids Surf B Biointerfaces* 2020, **187:** 110609.

12. Seddon AM, Curnow P, Booth PJ. Membrane proteins, lipids and detergents: not just a soap opera. *Biochim Biophys Acta* 2004, **1666**(1-2)**:** 105-117.

13. Lichtenberg D, Ahyayauch H, Goni FM. The mechanism of detergent solubilization of lipid bilayers. *Biophys J* 2013, **105**(2)**:** 289-299.

14. Sudbrack TP, Archilha NL, Itri R, Riske KA. Observing the solubilization of lipid bilayers by detergents with optical microscopy of GUVs. *J Phys Chem B* 2011, **115**(2)**:** 269-277.

15. Mattei B, Lira RB, Perez KR, Riske KA. Membrane permeabilization induced by Triton X-100: The role of membrane phase state and edge tension. *Chem Phys Lipids* 2017, **202:** 28-37.

16. Casadei BR, Domingues CC, de Paula E, Riske KA. Direct visualization of the action of Triton X-100 on giant vesicles of erythrocyte membrane lipids. *Biophys J* 2014, **106**(11)**:** 2417-2425.

17. Mattei B, Franca AD, Riske KA. Solubilization of binary lipid mixtures by the detergent Triton X-100: the role of cholesterol. *Langmuir* 2015, **31**(1)**:** 378-386.

18. Dalgarno PA, Juan-Colas J, Hedley GJ, Pineiro L, Novo M, Perez-Gonzalez C*, et al.* Unveiling the multi-step solubilization mechanism of sub-micron size vesicles by detergents. *Sci Rep* 2019, **9**(1)**:** 12897.

19. Drab M, Pandur Z, Penic S, Iglic A, Kralj-Iglic V, Stopar D. A Monte Carlo study of giant vesicle morphologies in nonequilibrium environments. *Biophys J* 2021, **120**(20)**:** 4418-4428.

20. Aleksanyan M, Faizi HA, Kirmpaki MA, Vlahovska PM, Riske KA, Dimova R. Assessing membrane material properties from the response of giant unilamellar vesicles to electric fields. *Adv Phys X* 2023, **8**(1).

21. Arnulphi C, Sot J, Garcia-Pacios M, Arrondo JLR, Alonso A, Goni FM. Triton X-100 partitioning into sphingomyelin Bilayers at subsolubilizing detergent concentrations: Effect of lipid phase and a comparison with Dipalmitoylphosphatidylcholine. *Biophysical Journal* 2007, **93**(10)**:** 3504-3514.

22. Dezi M, Di Cicco A, Bassereau P, Levy D. Detergent-mediated incorporation of transmembrane proteins in giant unilamellar vesicles with controlled physiological contents. *Proc Natl Acad Sci U S A* 2013, **110**(18)**:** 7276-7281.

23. Skrzypek R, Iqbal S, Callaghan R. Methods of reconstitution to investigate membrane protein function. *Methods* 2018, **147:** 126-141.

24. Pizzirusso A, De Nicola A, Sevink GJA, Correa A, Cascella M, Kawakatsu T*, et al.* Biomembrane solubilization mechanism by Triton X-100: a computational study of the three stage model. *Phys Chem Chem Phys* 2017, **19**(44)**:** 29780-29794.

25. Marrink SJ, Mark AE. The mechanism of vesicle fusion as revealed by molecular dynamics simulations. *J Am Chem Soc* 2003, **125**(37)**:** 11144-11145.

26. Schamberger B, Ziege R, Anselme K, Ben Amar M, Bykowski M, Castro APG*, et al.* Curvature in Biological Systems: Its Quantification, Emergence, and Implications across the Scales. *Adv Mater* 2023, **35**(13)**:** e2206110.

27. Yoon TY, Okumus B, Zhang F, Shin YK, Ha T. Multiple intermediates in SNARE-induced membrane fusion. *Proc Natl Acad Sci U S A* 2006, **103**(52)**:** 19731-19736.

28. Diao J, Ishitsuka Y, Lee H, Joo C, Su Z, Syed S*, et al.* A single vesicle-vesicle fusion assay for in vitro studies of SNAREs and accessory proteins. *Nat Protoc* 2012, **7**(5)**:** 921-934.

29. Dresser L, Graham SP, Miller LM, Schaefer C, Conteduca D, Johnson S*, et al.* Tween-20 Induces the Structural Remodeling of Single Lipid Vesicles. *J Phys Chem Lett* 2022, **13**(23)**:** 5341-5350.

30. Juan-Colas J, Dresser L, Morris K, Lagadou H, Ward RH, Burns A*, et al.* The Mechanism of Vesicle Solubilization by the Detergent Sodium Dodecyl Sulfate. *Langmuir* 2020, **36**(39)**:** 11499-11507.

31. Heerklotz H, Seelig J. Titration calorimetry of surfactant-membrane partitioning and membrane solubilization. *Biochim Biophys Acta* 2000, **1508**(1-2)**:** 69-85.

32. Elsayed MMA, Ibrahim MM, Cevc G. The effect of membrane softeners on rigidity of lipid vesicle bilayers: Derivation from vesicle size changes. *Chem Phys Lipids* 2018, **210:** 98-108.

33. Francois-Martin C, Pincet F. Actual fusion efficiency in the lipid mixing assay - Comparison between nanodiscs and liposomes. *Sci Rep-Uk* 2017, **7**.

34. Tabouillot T, Muddana HS, Butler PJ. Endothelial Cell Membrane Sensitivity to Shear Stress is Lipid Domain Dependent. *Cell Mol Bioeng* 2011, **4**(2)**:** 169-181.

35. Lee IH, Saha S, Polley A, Huang H, Mayor S, Rao M*, et al.* Live cell plasma membranes do not exhibit a miscibility phase transition over a wide range of temperatures. *J Phys Chem B* 2015, **119**(12)**:** 4450-4459.

36. Streletzky K, Phillies GDJ. Temperature-Dependence of Triton X-100 Micelle Size and Hydration. *Langmuir* 1995, **11**(1)**:** 42-47.

37. Kyoung M, Zhang Y, Diao J, Chu S, Brunger AT. Studying calcium-triggered vesicle fusion in a single vesicle-vesicle content and lipid-mixing system. *Nat Protoc* 2013, **8**(1)**:** 1-16.

38. Flagmeier P, De S, Wirthensohn DC, Lee SF, Vincke C, Muyldermans S*, et al.* Ultrasensitive Measurement of Ca2+ Influx into Lipid Vesicles Induced by Protein Aggregates. *Angew Chem Int Edit* 2017, **56**(27)**:** 7750-7754.

39. Daily NJ, Santos R, Vecchi J, Kemanli P, Wakatsuki T. Calcium Transient Assays for Compound Screening with Human iPSC-derived Cardiomyocytes: Evaluating New Tools. *J Evol Stem Cell Res* 2017, **1**(2)**:** 1-11.

40. Allolio C, Harries D. Calcium Ions Promote Membrane Fusion by Forming Negative-Curvature Inducing Clusters on Specific Anionic Lipids. *ACS Nano* 2021, **15**(8)**:** 12880-12887.

41. Schmid YRF, Scheller L, Buchmann S, Dittrich PS. Calcium-Mediated Liposome Fusion to Engineer Giant Lipid Vesicles with Cytosolic Proteins and Reconstituted Mammalian Proteins. *Adv Biosyst* 2020, **4**(11)**:** e2000153.

42. Dresser L, Hunter P, Yendybayeva F, Hargreaves AL, Howard JAL, Evans GJO*, et al.* Amyloid-beta oligomerization monitored by single-molecule stepwise photobleaching. *Methods* 2021, **193:** 80-95.

43. Chlanda P, Mekhedov E, Waters H, Schwartz CL, Fischer ER, Ryham RJ*, et al.* The hemifusion structure induced by influenza virus haemagglutinin is determined by physical properties of the target membranes. *Nat Microbiol* 2016, **1**(6).

44. Ward AE, Kiessling V, Pornillos O, White JM, Ganser-Pornillos BK, Tamm LK. HIV-cell membrane fusion intermediates are restricted by Serincs as revealed by cryo-electron and TIRF microscopy. *J Biol Chem* 2020, **295**(45)**:** 15183-15195.

45. Quinn SD, Dresser L, Graham S, Conteduca D, Shepherd J, Leake MC. Crowding-induced morphological changes in synthetic lipid vesicles determined using smFRET. *Front Bioeng Biotechnol* 2022, **10:** 958026.

46. Morandi MI, Busko P, Ozer-Partuk E, Khan S, Zarfati G, Elbaz-Alon Y*, et al.* Extracellular vesicle fusion visualized by cryo-electron microscopy. *PNAS Nexus* 2022, **1**(4)**:** pgac156.

47. Nomura F, Nagata M, Inaba T, Hiramatsu H, Hotani H, Takiguchi K. Capabilities of liposomes for topological transformation. *Proc Natl Acad Sci U S A* 2001, **98**(5)**:** 2340-2345.

48. Staneva G, Seigneuret M, Koumanov K, Trugnan G, Angelova MI. Detergents induce raft-like domains budding and fission from giant unilamellar heterogeneous vesicles: a direct microscopy observation. *Chem Phys Lipids* 2005, **136**(1)**:** 55-66.

49. Tomita T, Sugawara T, Wakamoto Y. Multitude of morphological dynamics of giant multilamellar vesicles in regulated nonequilibrium environments. *Langmuir* 2011, **27**(16)**:** 10106-10112.

50. Abraham S, Heckenthaler T, Bandyopadhyay D, Morgenstern Y, Kaufman Y. Quantitative Description of the Vesicle Fusion Mechanism on Solid Surfaces and the Role of Cholesterol. *J Phys Chem C* 2018, **122**(40)**:** 22985-22995.

51. Stetefeld J, McKenna SA, Patel TR. Dynamic light scattering: a practical guide and applications in biomedical sciences. *Biophys Rev* 2016, **8**(4)**:** 409-427.

52. Preus S, Noer SL, Hildebrandt LL, Gudnason D, Birkedal V. iSMS: single-molecule FRET microscopy software. *Nat Methods* 2015, **12**(7)**:** 593-594.